

Magnetic properties of graphene nanodisk and nanocone powders at low temperatures

Jozef Černák*

Department of Nuclear and Sub-Nuclear Physics, Institute of Physics, Faculty of Sciences, P. J. Šafárik Univesity in Košice, Jesenná 5, SK-04001 Košice, Slovak Republic

Geir Helgesen

Physics Department, Institute for Energy Techology, NO-2027 Kjeller, Norway

Erik Čižmár

Department of Condensed Matter Physics, Institute of Physics, Faculty of Sciences, P. J. Šafárik Univesity in Košice, Park Angelinum 9, SK-04001 Košice, Slovak Republic

Jozef Kováč

Laboratory of Nanomaterials and Applied Magnetisms, Institute of Physics, Slovak Academy of Sciences, Watsonova 47, SK-04001 Košice, Slovak Republic

Zuzana Jurašeková

Department of Biophysics and Center for Interdisciplinary Biosciences, Institute of Physics, Faculty of Sciences, P. J. Šafárik Univesity in Košice, Jesenná 5, SK-04001 Košice, Slovak Republic

Josef Voltr

Faculty of Nuclear Sciences and Physical Engineering, Czech Technical University in Prague, Břehová 7, CZ-11519 Praha 1, Czech Republic

(Received 26 June 2015; revised manuscript received 19 August 2015; published 23 October 2015)

Our aim is the study of magnetization phenomena of carbon powders consisting of graphene nanocones and nanodisks. Magnetization measurements were carried out using a superconducting quantum interference device in magnetic fields $-5 < B < 5$ T for temperatures in the range $0.5 \leq T < 300$ K. We have observed that magnetization M depends on temperature T as a power law $M \propto T^{-\alpha}$ where the scaling exponent $\alpha = 0.79 \pm 0.04$ was determined. We found that the magnetization consists of a diamagnetic background and a paramagnetic contribution of localized spins. Considering saturation magnetization M_S in the free spin magnetization model and diamagnetic susceptibility χ_D for independent of temperature T we found that the effective spin value S increases from $S = 1/2$ at temperature $T > 20$ K to $S = 3$ at low temperatures $0.5 \leq T \leq 20$ K.

DOI: [10.1103/PhysRevB.92.155429](https://doi.org/10.1103/PhysRevB.92.155429)

PACS number(s): 75.20.Ck

I. INTRODUCTION

Study of the magnetic properties of graphene [1] and multilayer graphene stacks at low temperatures is one of the methods which can shed light on quantum spin interactions in Dirac-like systems and may pave a road to new applications [2]. Carbon allotropes show diamagnetism [3], paramagnetism [4], ferromagnetism [5–7], and antiferromagnetism [8] whereby a carbon sample may show a magnetization consisting of a mixture of the previous effects. For example, point defects in graphene laminates [9] induce additional spin-half paramagnetism to basal diamagnetism.

First-principles calculations [10] predicted that vacancy defects could induce either ferromagnetic or antiferromagnetic interactions. In highly ordered pyrolytic graphite (HOPG) samples irradiated by protons, ferromagnetic order was found using magnetization measurements [6] and the x-ray dichroism method [7]. However, HOPG samples irradiated by neutrons [11], where point defects are close enough to create long-ranged ferromagnetic ordering, showed free spin paramagnetism [4,9]. Recent experiments using controlled

zigzag edges of narrow graphene nanoribbons [5] show magnetic ordering of spins at the nanoscale.

Spin-half paramagnetism and Curie law induced by point defects were observed in carbon samples [4,9,11]. Our study of raw carbon nanopowder (denoted HT-0) [12] shows paramagnetic behavior, and a spin-half paramagnetic approximation of magnetization is possible at low temperature $T = 2$ K. However, magnetization M vs temperature T deviates from the expected Curie law. To verify the spin-half paramagnetic approximation at low temperatures $T < 2$ K as well as the validity of the Curie law in the case of a sample containing fewer defects and less density of unpaired spins we investigated the properties of carbon nanoparticles which were heat treated to reduce the density of defects [8].

Magnetization measurements are analyzed and discussed considering an influence of residual metallic impurities, which were determined by the PIXE method, and the inner structure of nanoparticles. The nanoparticles consists of graphene stacked in three-dimensional (3D) nanocrystallites with a form and average size which were determined by Raman spectroscopy [13] and x-ray diffraction.

The paper is organized as follows. In Sec. II we characterize carbon nanoparticles, content of metallic impurities in carbon powder, as well as in-plane size of graphene nanocrystallites.

*jozef.cernak@upjs.sk

Magnetization measurements are shown in Sec. III. The results are discussed in Sec. IV followed by conclusions in Sec. V.

II. SAMPLE CHARACTERIZATION

A. Carbon nanoparticles

The graphiticlike carbon powder [14] used in this study was produced in an industrial, pyrolytic process that decomposes hydrocarbons into hydrogen and carbon using a plasma torch at temperatures above 2000 °C [15]. In order to improve the crystalline quality of the particles, i.e., to reduce density of structural defects, additional annealing was done by heating the powder to high temperatures in an argon atmosphere for 3 h followed by a slow natural cooling. The powder consists of flat nanocarbon disks (70%), open-ended carbon cones (20%), and a small amount of carbon black [14,16,17]. The carbon disks and cones exhibit diameters in the range 500–4000 nm having wall thickness of typically 10–30 nm. Transmission electron microscopy (TEM) diffraction patterns show that these particles are multilayer carbon structures with a graphiticlike core and outer noncrystalline layers [16,18]. It was reported by Krishnan *et al.* [14] that the carbon powder consisted of perfect carbon nanocones of five possible apex angles in the range 112.9° – 19.2°, corresponding to $n = 1$ –5 carbon pentagonal rings near the cone tip. The flat disks can be considered as cones with $n = 0$. High-resolution TEM [19] shows the growth of the inner graphitic core with increasing annealing temperature starting from 10–30% of the disk thickness in the as-produced particles. Previous studies of structural properties of these nanocarbon powders have reported for the current samples a coherence length along the crystalline c axis of 4.5 ± 0.8 nm [20]. Samples heat treated at 1600 °C (denoted HT-1600) have been characterized as metallic, with a weak Anderson localization and antilocalization of charge carriers, and with 2D graphenelike electronic transport [20].

B. Metallic impurities in carbon powder

In order to determine any small trace of impurity elements in our carbon samples we used proton induced x-ray analysis (PIXE) [21]. PIXE is a very useful tool for determination of concentrations of trace elements in small quantities of material. It is often used for analysis of aerosol samples, where air dust or aerosol particulates are collected on the membrane filters and has also been used for the determination of the impurities (Fe, Cr, and others) in the carbon powders. The material was fixed on Cyclopore polycarbonate membranes of diameter 25 mm with pore size 5 μm . Pure membrane was weighed (Mettler Toledo) first, and then material was deposited on a spot of diameter 5 mm and the sample was weighed again. The weight differences, i.e., amounts of the carbon material, were in the range 0.1–0.2 mg. Taking into account the density of amorphous carbon, about 2000 kgm^{-3} , the thickness of the deposit was in the range 2–4 μm . For proton beam energy of 2 MeV and thin targets, the protons penetrate through the samples with negligible loss of energy.

The PIXE analyses were performed in the ion beam facility of the Czech Technical University. A proton beam of energy 2 MeV was obtained from a Van de Graaff accelerator. Diameter of the beam spot on the target was 8 mm, so all

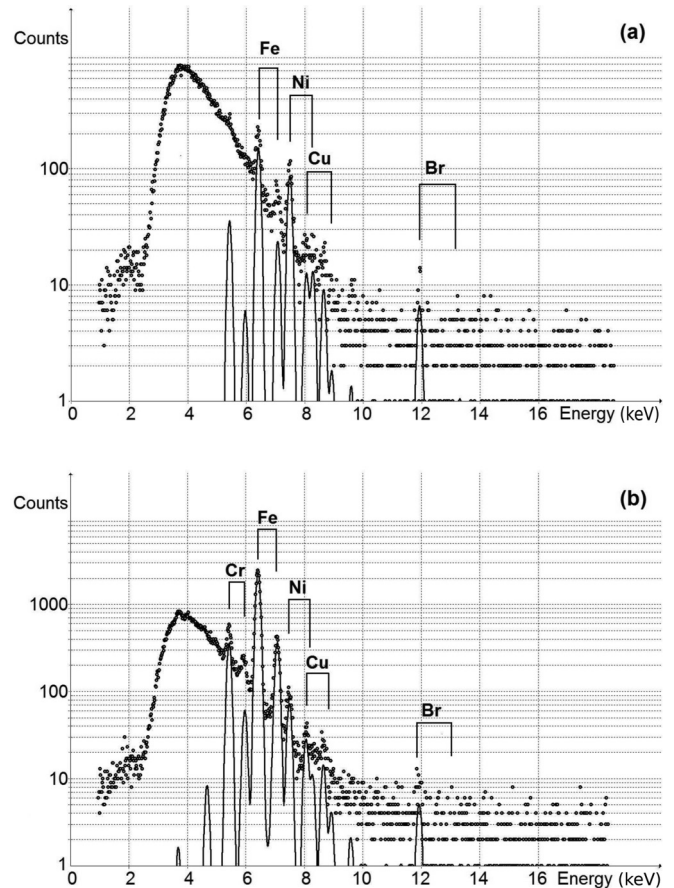


FIG. 1. PIXE spectra of (a) the pure Cyclopore membrane and (b) typical PIXE spectra of HT-1600 carbon powder on a Cyclopore membrane.

carbon material on the sample was irradiated. Homogeneity of the beam was tested by a cylindrical probe. Samples were placed perpendicular to the beam axis, and a Si(Li) detector was collecting x rays in a sector of angle 60°. In order to attenuate the low-energy part of the spectra, a foil of Mylar with thickness 356 μm was placed in front of the detector. For calibration, MicroMatter thin standard Fe was used. As the samples were thin, beam current was measured by a Faraday cup behind the sample. Exposition fluences were about 50 μC . In the same way, the original Cyclopore membranes were analyzed to check their purity. Spectra were calculated by the GUPIXWIN software package [22]. An example of PIXE spectrum of a pure filter is shown in Fig. 1(a) and an example of the sample with carbon powder is shown in Fig. 1(b). Dotted lines are measured data and solid lines are fitted peaks belonging to relevant lines of the elements. A background with the top energy of 3.7 keV originates mainly from bremsstrahlung. X-ray energies smaller than this value are rapidly suppressed by the foil in front of the detector. From this analysis we conclude that the concentration of iron in the carbon powders was found to be 60 ± 15 μg of Fe per 1 g of carbon. There was also a very small amount of Cr in the material, 8 ± 4 μg of Cr per 1 g of carbon. The polycarbonate membrane contains a residual amount of Ni shown in Figs. 1(a) and 1(b), however Ni contamination of carbon powder itself is under the detection limit of the PIXE method. Accuracy

of the result is also influenced by the impurities (Fe, Ni, and Cu) in the polycarbonate membranes. The density of metallic impurities in these HT-1600 samples is comparable to that of the as-produced, raw material HT-0 [12].

C. In-plane crystallite size of graphene nanocrystallites

Raman spectra [13] can be useful to determine in-plane crystallite size L_a by applying the empirical relation [23]

$$L_a = \frac{4.4}{R} \left(\frac{2.41}{E_L} \right)^4 \quad (\text{nm}), \quad (1)$$

where R is the ratio of integrated intensities for the D and G Raman lines, $R = I_D/I_G$, and E_L is the excitation energy used, in our case $E_L = 2.33$ eV. We note that the in-plane crystallite size of the HT-1600 powder $L_a = 4.5$ nm calculated by using Eq. (1) and the coherence length along the c axis, $L_c = 4.5 \pm 0.8$ nm determined from an x-ray study [20], are almost identical.

III. MAGNETIZATION MEASUREMENT

We measured magnetization M vs temperature T in the range $0.5 \leq T < 300$ K, magnetization M vs magnetic field (magnetic flux density) B in the range $-5 \leq B \leq 5$ T. Magnetization measurements were carried out using a Quantum Design superconducting quantum interference device (SQUID) Magnetic Properties Measurement System (MPMS) and the sub-2-K iHelium3 insert for MPMS. Before each measurement we used a procedure to evaporate oxygen and vapors from the SQUID chamber to avoid effects of absorbed gases on the measurements. Magnetization data were carefully corrected considering the magnetization of the sample holder (gelatin capsule) and residual metallic impurities in the carbon powder in order to obtain the pure magnetization that is attributed to the carbon powder itself. We measured several samples, however, here we present the results of one typical sample.

A clear detection of the carbon magnetization is possible after careful removal of the signals from the metallic contamination (see below), mainly from Fe [9,12]. The saturation magnetization of metallic impurities in the HT-1600 powder is five times smaller than the saturation magnetization of the impurities in the raw material HT-0 reported previously [12] and it is much smaller than the saturation magnetization of the carbon in the sample. Therefore, we attribute the magnetic properties at low temperatures of this sample to be due to changing electronic properties of the carbon nanoparticles rather than to the metallic contamination.

A. Magnetization vs temperature measurements

The temperature dependence of the zero-field-cooled M_{ZFC} and field-cooled magnetization M_{FC} are shown in Fig. 2 for the external magnetic field $B = 0.1$ T. The magnetizations M_{ZFC} and M_{FC} are corrected also taking into account the diamagnetism of carbon, and the capsule magnetization, which was measured in the same magnetic field in the temperature range $0.5 \leq T < 300$ K. The graphs of magnetization M_{ZFC} could be approximated by a function $M(T) = aT^{-\alpha} + b$, where $a = (4.49 \pm 0.11) \times 10^{-3} \text{ A m}^2 \text{ kg}^{-1}$, $\alpha =$

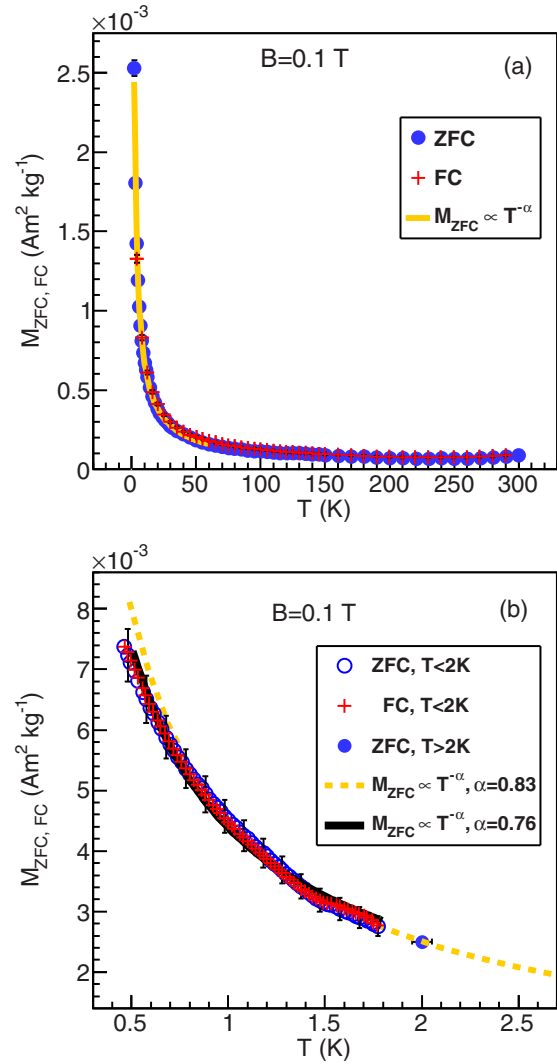


FIG. 2. (Color online) Magnetizations M_{ZFC} and M_{FC} vs temperature T in magnetic field $B = 0.1$ T after metallic impurity, gelatine capsule magnetizations, and the diamagnetic background are subtracted. (a) Magnetization M_{ZFC} follows the power law $M_{ZFC} \propto T^{-\alpha}$, $\alpha = 0.83 \pm 0.02$, for temperature $1.8 \leq T < 60$ K. (b) Magnetization M_{ZFC} at low temperature $T < 1.8$ K follows the power law $M_{ZFC} \propto T^{-\alpha}$ with exponent $\alpha = 0.76 \pm 0.05$.

0.83 ± 0.02 , $b = -0.93 \times 10^{-3} \text{ A m}^2 \text{ kg}^{-1}$ for $1.8 < T < 60$ K and $a = (4.6 \pm 0.17) \times 10^{-3} \text{ A m}^2 \text{ kg}^{-1}$, $\alpha = 0.76 \pm 0.05$, $b = -0.95 \times 10^{-3} \text{ A m}^2 \text{ kg}^{-1}$ for lower temperatures ($0.5 \leq T \leq 1.8$ K). We observed that magnetization does not depend on the cooling procedure within measurement accuracy because $M_{ZFC} \doteq M_{FC}$ in the broad temperature range $0.5 \leq T < 300$ K.

B. Magnetization vs magnetic-field measurements

The full magnetization loops in Fig. 3 measured at temperatures in the range $0.5 \leq T < 50$ K, after diamagnetic background corrections of the experimental data, are shown in Fig. 4. The magnetization loops were analyzed using the noninteracting spin model where the magnetization is described by the Brillouin function, which is based on

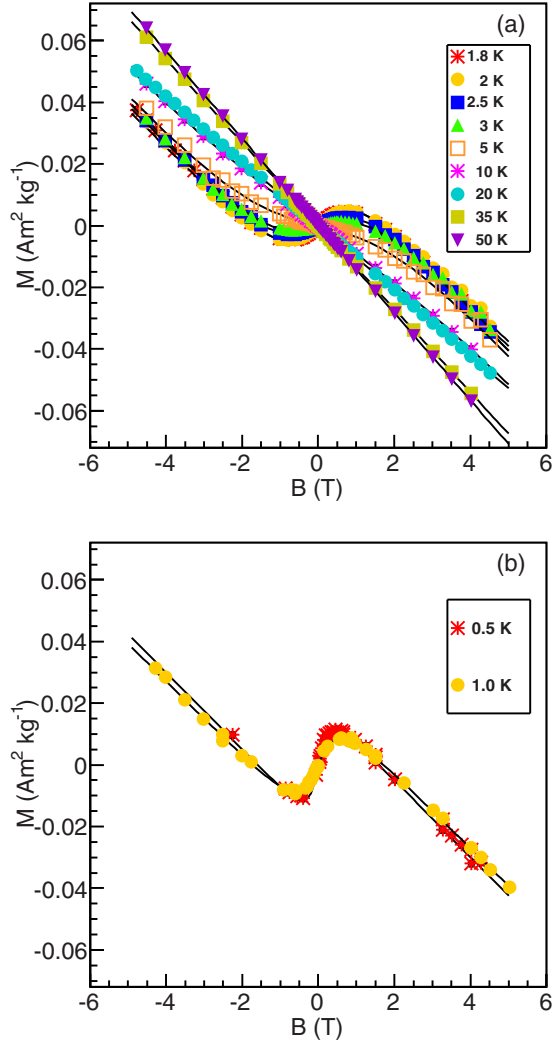


FIG. 3. (Color online) Curves for carbon magnetization M vs magnetic field B for temperature (a) $T \geq 1.8$ K and (b) $T = 0.5$ and 1.0 K. The data shown here have been corrected by subtracting measured magnetization of the gelatine capsule and of metallic impurities from the measured carbon sample data. The solid lines represent fits of the experimental data considering effects of diamagnetic and paramagnetic free spin magnetizations [Eqs. (4) and (5)].

the assumption that the population of energy levels obeys Boltzmann statistics [24].

The isothermal magnetization loop at temperature $T = 300$ K showed a diamagnetic background magnetization $M_D(B) = \frac{B}{\mu_0} \chi_D$ and in addition a nonlinear magnetization $M_{T=300\text{ K}}(B)$. The magnetization $M_{T=300\text{ K}}(B)$ was approximated by a Brillouin function $M/M_S = B_S(x)$, where the Brillouin function $B_S(x)$ is given by

$$B_S(x) = \frac{2S+1}{2S} \coth\left(\frac{2S+1}{2S}x\right) - \frac{1}{2S} \coth\left(\frac{1}{2S}x\right) \quad (2)$$

with $x = g\mu_B BS/k_B T$, S is the spin value, g is the Landé factor, μ_B is the Bohr magneton, and k_B is the Boltzmann constant. The saturation magnetization M_S is given by

$$M_S = Ng\mu_B S, \quad (3)$$

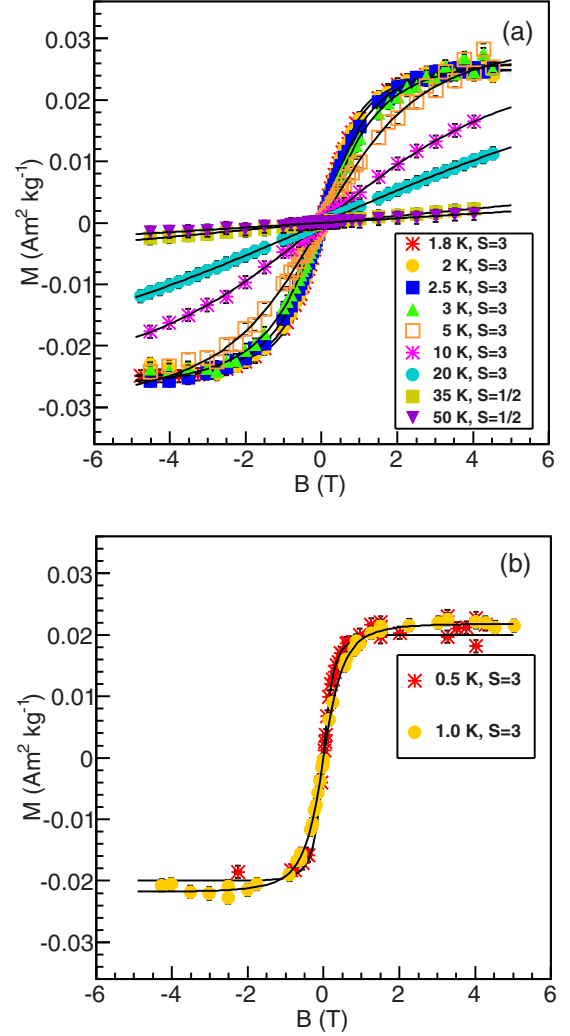


FIG. 4. (Color online) Magnetization M vs magnetic field B at selected temperatures in the intervals (a) $1.8 \leq T < 50$ K and (b) $T = 0.5$ and 1 K. Here, the magnetization of the gelatin capsule, the ferromagnetic background of metallic impurities, and the diamagnetic background of the carbon powder have been subtracted from the measured data. Solid lines show approximations to these corrected data based on Eq. (2). For each temperature, the value of S that gave the best fit is shown.

where N is the number of magnetic moments per unit volume. Since the magnetization does not reach saturation at high temperatures, we made the assumption that the saturation magnetization was independent of temperature, which in the current model means that the total number of spins is fixed.

Assuming that the only contribution to magnetization at room temperature (after subtraction of the diamagnetic background) is associated with residual metallic elements, mainly Fe, we estimate $M_{S,T=300\text{ K}} = (10.65 \pm 1.35) \times 10^{-4} \text{ A m}^{-2} \text{ kg}^{-1}$, as a temperature-independent ferromagnetic background signal. This value is consistent with the ferromagnetic background found at all the lower temperatures. Therefore, the isothermal magnetization loop $M_{T=300\text{ K}}(B)$ could be subtracted from all experimental isothermal loops for $T < 300$ K. Experimental data after subtraction of the residual impurity magnetization at $T = 300$ K, $M_{T=300\text{ K}}(B)$, and the

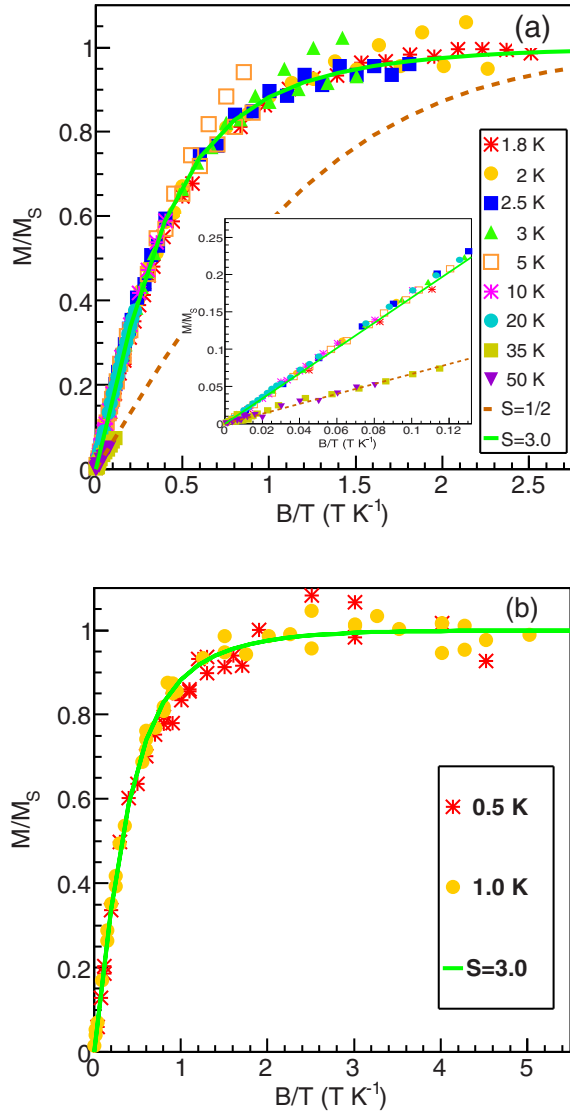


FIG. 5. (Color online) M/M_S vs B/T plots for temperatures (a) $1.8 \leq T \leq 50$ K and (b) $T = 0.5$ and 1 K. Solid lines show approximations to these corrected data based on Eq. (2) using either $S = \frac{1}{2}$ or $S = 3$. The inset shows a detail near origin of coordinate axes.

capsule magnetization are shown in Fig. 3. The removal of the isothermal magnetization loop $M_{T=300\text{ K}}(B)$ is similar to the approach used in previous studies [11,12].

The isothermal magnetization loops shown in Fig. 3 were analyzed using ROOT software [25]. Graphs of magnetization M vs magnetic field B were approximated by Eqs. (4) and (5),

$$M = M_S B_S(x) + \frac{B}{\mu_0} \chi_D, \quad (4)$$

$$x = g\mu_B BS/k_B T, \quad (5)$$

where the carbon saturation magnetization M_S , spin number S , and diamagnetic susceptibility χ_D were parameters.

At low temperatures $0.5 \leq T < 2$ K where magnetization saturates these fitting parameters were free. At higher temperatures $T \geq 2$ K the parameter S was limited $0.5 \leq S \leq 3$

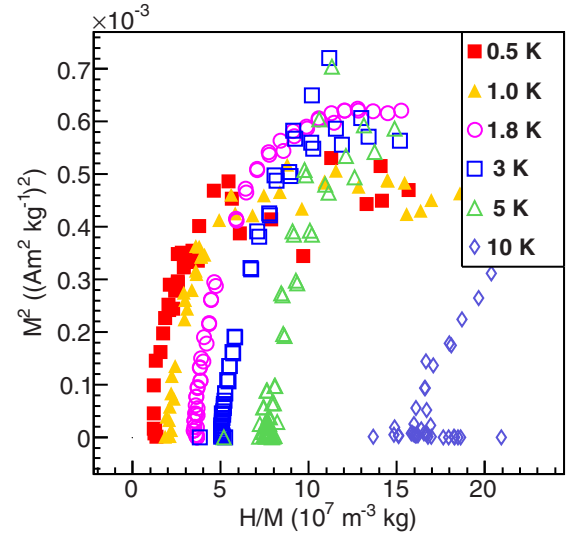


FIG. 6. (Color online) Arrott plots of the background corrected data in the temperature range $0.5 \leq T \leq 10$ K.

and parameters M_S and χ_D were fixed to values which were determined for low-temperature magnetization loops. We assume that the number of defects in the carbon structure that induce magnetization M_S , as well as the diamagnetic susceptibility χ_D , are independent of temperature. Considering that the magnetization $M_S \gg M_{S,T=300\text{ K}}$, we believe that the magnetization M is intrinsic to the carbon powder.

Applying a fitting procedure based on Eqs. (4) and (5) to the experimental data, we determined the saturation magnetization M_S and diamagnetic mass susceptibility χ_D as follows: $M_S = (0.024 \pm 0.003)$ A m² kg⁻¹, $\chi_D = -(17 \pm 1.2) \times 10^{-9}$ m³ kg⁻¹ for $0.5 \leq T < 60$ K. These values were used for making the corrected data in Fig. 4. Isothermal magnetization loops from Fig. 4 were replotted in Fig. 5 to verify the validity of the free-spin magnetization model. If all isothermal magnetization loops fall onto a single curve, then the model is assumed to be valid. Taking into account that $g = 2.0$ [12,26], and assuming that saturation magnetization M_S and diamagnetic susceptibility χ_D are independent of temperature, consistent fits can only be obtained if we allow the spin value S to be temperature dependent, with $S = 1/2$ for $T > 20$ K and $S = 3$ for $0.5 \leq T \leq 20$ K.

Assuming homogeneously distributed spins and using Eq. (3), we estimate a spin density $n = 3.0 \times 10^{18}$ g⁻¹, which corresponds to an average separation of spins $\langle r \rangle = 5$ nm at temperatures $T > 20$ K.

In order to further check the paramagnetic nature of the sample, we made Arrott plots [27], M^2 vs $\frac{H}{M}$, which are shown in Fig. 6. The plots show the paramagnetic nature of the samples with no indication of a phase transition.

IV. DISCUSSION

The HT-1600 sample shows similar diamagnetic behavior as the raw material powder HT-0 [12] with diamagnetic susceptibility $\chi_D = -17 \times 10^{-9}$ m³ kg⁻¹. In order to compare the absolute value of the diamagnetic susceptibility $|\chi_D|$

of our samples to that measured by Sepioni *et al.* [4] for graphene laminates, one may calculate a weighted average of $|\chi_D^{\parallel}|$ and $|\chi_D^{\perp}|$ (the in-plane and normal component) reported for the graphene laminates. This absolute value, about $35 \times 10^{-9} \text{ m}^3 \text{ kg}^{-1}$, is two times the $|\chi_D|$ found in our samples.

In the free spin model of magnetization, M vs T follows the Curie law. The graphs in Fig. 2 show similarities to ordinary paramagnetism, however we were not successful in fitting the magnetization M to a Curie law behavior $M = C/T$ where C is the Curie constant [4,8,9,11]. We found that the magnetization of the HT-1600 sample follows rather $M \propto T^{-\alpha}$ where the exponent $\alpha < 1$. Similar observations were reported earlier for the raw powder HT-0 sample [12], and also for doped semiconductors, certain rare-earth intermetallics, and insulating magnetic salts [28]. The exponent $\alpha < 1$ indicates that there are magnetic spin interactions. Spatially random Heisenberg spins in 3D space with antiferromagnetic coupling that interact through an exponentially decaying interaction vs separation [29] show an exponent $\alpha < 1$. The exponent $\alpha < 1$ was also found in insulating magnetic salts where there is an entangled quantum state of magnetic dipoles [28]. In this entangled quantum state, the spins do not have a tendency to freeze and magnetic susceptibility increases with decreasing temperature down to extremely low temperatures, but at a rate slower than the Curie law [28]. We also observe a tendency to increasing magnetization at low temperatures with a rate slower than the Curie law (Fig. 2), however the current results do not allow us to make a conclusion about possible entanglement of spins. Magnetization measurements at ultralow temperatures (near 10 mK) are needed to demonstrate a nonfreezing state of spins together with a magnetization exponent $\alpha < 1$.

Magnetization loops (Fig. 4) are well approximated by the Brillouin functions especially at $B/T < 1$ (Fig. 5), i.e., the spin response on changing magnetic field is paramagnetic. The Arrott plots show the same paramagnetic property with no indication of a phase transition. For temperature $T > 20$ K, the spin number $S = 1/2$ agrees well with the earlier results from an as-produced material sample (HT-0) [12] at $T = 2$ K, and is also consistent with results from carbon based materials with induced point defects [9,11]. Assuming that saturation magnetization M_S and diamagnetic susceptibility χ_D are temperature independent, then the effective spin value S increases below $T = 20$ K where $S = 3$. Higher spin numbers S , i.e., $S = 2$ and $S = 5/2$ (at $g = 2$ and $2 \leq T \leq 50$ K) than $S = 1/2$ were reported for laminates [4] consisting of mono- and bilayer crystallites with typical sizes of 10 – 50 nm. The origin of such high values of S in the graphene laminates has not been clarified [4]. In our case, for multilayer graphene crystallites with a size of ~ 5 nm, the results show the high effective spin value $S = 3$ below $T = 20$ K, and a transition from $S = 1/2$ to $S = 3$ with decreasing temperature, which has not been reported for the laminates [4]. The authors [4] observed a reduction in magnetization M for large crystallites, i.e., the size of graphene crystallites is an important structural factor that influences magnetization M . Our measured saturation magnetizations of HT-0 [12] and HT-1600 samples are consistent with this finding.

We know that the planar L_a size, the c -axis coherence length L_c , and the average distance $\langle r \rangle$ among spins are comparable in size. Thus, the current spin density corresponds to just a few single unpaired spins per nearly crystalline graphene-layer unit of volume $\sim L_a^2 L_c$, and these spins will likely be located at the surfaces or grain boundaries of these crystalline graphene layer units. The existence of such edge states [30,31] and zigzag segments [4] on the graphitic nanocrystals can modify the electronic band structure at low temperatures and can introduce some coupling among spins in a single graphene layer, or across layers. Recently it was reported [32] that multilayer graphene nanoribbons show a linear temperature dependence of the linewidth of electron spin resonance (ESR) signal, which indicates a coupling between conduction π electron carriers and edge-state spins. One may speculate that a similar coupling may occur in our samples at low temperatures, and that this coupling may “dress” the defect edge-state spins by properties from the π -band electrons, giving rise to the observed increase in the effective spin value. Further ESR measurement will be needed to confirm this. It could be a probable alternative explanation that the effective spin $S = 3$ is a consequence of a coherent behavior of six unpaired spins at low temperatures.

Since the 3D nanocrystallites are randomly oriented inside the carbon particles and the particles are randomly packed in a sample, there is no long-range ordering of spins that can give rise to ferromagnetism. Macroscopically, the unpaired spins form an open 3D random network. Taking into account the large surface area and the presumably large number of grain boundaries and defects in this material, the average density of unpaired spins is relatively low, similar to what was reported for graphene laminates [4]. We characterize the magnetization process as paramagnetic despite the fact that the unpaired spins are close enough [11] to be ordered antiferromagnetically [8] or ferromagnetically [6,7,10]. We have observed the signature of coherent behavior of a few unpaired spins in small volumes, however the magnetic order is not extended into the whole sample.

V. CONCLUSIONS

We conclude that free, unpaired spins possibly located at the edges and zigzag segments of graphenelike nanocrystallites show paramagnetic behavior down to low temperatures but with an exponent $\alpha < 1$. However, future experimental studies at ultralow temperatures are needed in order to look for any tendency of freezing out of these spins. Assuming a fixed number of unpaired spins and a fixed saturation magnetization, the isothermal magnetization loops can only be modeled consistently by changing the effective spin value from $S = 1/2$ to $S = 3$ at low temperatures.

ACKNOWLEDGMENTS

The authors would like to thank J. P. Pinheiro of n-Tec AS for providing the samples used in this study. This work was supported by SAS Centre of Excellence: CFNT MVEP, VEGA 1/0145/13, Research Council of Norway Grant No. 191621/F20, Institutional Research Plan MSM6840770040, and EU FP7-REGPOT Project No. 316310 (CELM).

- [1] A. H. Castro Neto, F. Guinea, N. M. R. Peres, K. S. Novoselov, and A. K. Geim, *Rev. Mod. Phys.* **81**, 109 (2009).
- [2] J. H. Warner, F. Scha, A. Bachmatiuk, and M. H. Rummeli, *Graphene Fundamentals and Emergent Applications* (Elsevier, Oxford, 2013).
- [3] R. C. Haddon, *Nature (London)* **378**, 249 (1995).
- [4] M. Sepioni, R. R. Nair, S. Rablen, J. Narayanan, F. Tuna, R. Winpenny, A. K. Geim, and I. V. Grigorieva, *Phys. Rev. Lett.* **105**, 207205 (2010).
- [5] G. Z. Magda, X. Jin, I. Hagymási, P. Vancsó, Z. Osváth, P. Nemes-Incze, C. Hwang, L. P. Biró, and L. Tapasztó, *Nature (London)* **514**, 608 (2014).
- [6] P. Esquinazi, D. Spemann, R. Höhne, A. Setzer, K. H. Han, and T. Butz, *Phys. Rev. Lett.* **91**, 227201 (2003).
- [7] H. Ohldag, P. Esquinazi, E. Arenholz, D. Spemann, M. Rothermel, A. Setzer, and T. Butz, *New J. Phys.* **12**, 123012 (2010).
- [8] Y. Shibayama, H. Sato, T. Enoki, and M. Endo, *Phys. Rev. Lett.* **84**, 1744 (2000).
- [9] R. R. Nair, M. Sepioni, I.-L. Tsai, O. Lehtinen, J. Keinonen, A. V. Krasheninnikov, T. Thomson, A. K. Geim, and I. V. Grigorieva, *Nat. Phys.* **8**, 199 (2012).
- [10] O. V. Yazyev and L. Helm, *Phys. Rev. B* **75**, 125408 (2007).
- [11] Y. Wang, P. Pochet, C. A. Jenkins, E. Arenholz, G. Bukalis, S. Gemming, M. Helm, and S. Zhou, *Phys. Rev. B* **90**, 214435 (2014).
- [12] J. Černák, G. Helgesen, A. T. Skjeltorp, J. Kováč, J. Voltr, and E. Čížmár, *Phys. Rev. B* **87**, 014434 (2013).
- [13] See Supplemental Material at <http://link.aps.org/supplemental/10.1103/PhysRevB.92.155429> for Raman spectra of graphene nanodisk and nanocone powders.
- [14] A. Krishnan, E. Dujardin, M. M. J. Treacy, J. Higdahl, S. Lynum, and T. W. Ebbesen, *Nature (London)* **388**, 451 (1997).
- [15] J. Higdahl, K. Hox, S. Lynum, R. Hildrum, and M. Norvik, Norwegian Patent No. NO325686 (B1) (23 September 1999).
- [16] T. Garberg, S. N. Naess, G. Helgesen, K. D. Knudsen, G. Kopstad, and A. Elgsaeter, *Carbon* **46**, 1535 (2008).
- [17] H. Heiberg-Andersen, G. W. Walker, A. T. Skjeltorp, and S. N. Naess, in *Handbook of Nanophysics 5 - Functional Nanomaterials*, edited by K. D. Sattler (CRC, Boca Raton, FL, 2011), Chap. 25.
- [18] S. N. Naess, A. Elgsaeter, G. Helgesen, and K. D. Knudsen, *Sci. Technol. Adv. Mater.* **10**, 065002 (2009).
- [19] F. S. Hage, Ph.D. thesis, University of Oslo, 2013.
- [20] J. Černák, G. Helgesen, F. S. Hage, and J. Kováč, *J. Phys. D: Appl. Phys.* **47**, 335305 (2014).
- [21] S. A. E. Johansson, J. L. Campbell, and K. G. Malmqvist, *Particle-Induced X-ray Emission Spectroscopy (PIXE)* (John Wiley & Sons, New York, 1995).
- [22] <http://pixe.physics.uoguelph.ca/gupix/main/>.
- [23] P. Mallet-Ladeira, P. Puech, C. Toulouse, M. Cazayous, N. Ratel-Ramond, P. Weisbecker, G. L. Vignoles, and M. Monthieux, *Carbon* **80**, 629 (2014).
- [24] H. E. Stanley, *Introduction to Phase Transitions and Critical Phenomena* (Clarendon, Oxford, 1971).
- [25] A Data Analysis Framework: <https://root.cern.ch>.
- [26] ESR spectra of HT-1600 sample (unpublished).
- [27] A. S. Arrott, *J. Magn. Magn. Mater.* **322**, 1047 (2010).
- [28] S. Ghosh, T. F. Rosenbaum, G. Aeppli, and S. N. Coppersmith, *Nature (London)* **425**, 48 (2003).
- [29] R. N. Bhatt and P. A. Lee, *Phys. Rev. Lett.* **48**, 344 (1982).
- [30] K. Nakada, M. Fujita, G. Dresselhaus, and M. S. Dresselhaus, *Phys. Rev. B* **54**, 17954 (1996).
- [31] M. Wimmer, A. R. Akhmerov, and F. Guinea, *Phys. Rev. B* **82**, 045409 (2010).
- [32] V. L. J. Joly, M. Kiguchi, S.-J. Hao, K. Takai, T. Enoki, R. Sumii, K. Amemiya, H. Muramatsu, T. Hayashi, Y. A. Kim, M. Endo, J. Campos-Delgado, F. López-Urías, A. Botello-Méndez, H. Terrones, M. Terrones, and M. S. Dresselhaus, *Phys. Rev. B* **81**, 245428 (2010).